Power-efficient Near-field Focusing for Upcoming 6G MIMO Networks

Alessandro Felaco, Kamil Yavuz Kapusuz, *Member, IEEE*, Hendrik Rogier, *Senior Member, IEEE*, and Dries Vande Ginste, *Senior Member, IEEE*

***Abstract*—An accurate and efficient near-field intensity shaping method is proposed, capable of reproducing sharp patterns while simplifying the design requirements of the array's feeding network. The shaping problem is tackled by an efficient far-to-near-field transform, based on a spherical Fourier transform and multipole expansion of active radiation patterns, including mutual coupling effects. By limiting field levels outside the focussing region and by steering phases only, a power and cost-effective field shaping method is obtained. The added value of the advocated method is proven for the upcoming sixth-generation wireless networks with phase-only near-field shaping.**

***Index Terms*—Antenna arrays, focusing, harmonic analysis, near-field far-field transformation.**

I. Introduction

WITH the ever-growing size of antenna systems [1], owing, among others, to the emergence of extreme massive MIMO systems, the flexible control of electromagnetic (EM) fields in the radiative near-field [2], [3] of antenna arrays is essential in upcoming sixth-generation (6G) wireless networks to suppress interference from nearby scatterers, provide optimal radio coverage at minimum radiated power, and increase the wireless link reliability [4]. In particular, near-field shaping methods aim to generate a desired field intensity in a target area by optimizing the complex excitations of a large or distributed antenna array [5]. Yet, these conventional methods usually cannot ensure uniformity of the EM field in the target area while keeping the field intensity outside of it under control [6]. This may be tackled by steering each antenna element's amplitude using attenuators or gain-controlled amplifiers. Yet, this increases hardware cost and complexity [7], [8]. Hence, to avoid undesired field levels outside the target region while keeping the excitation network simple and cost-effective, new, simple near-field shaping methods must be devised with optimal performance and system cost.

This letter proposes a power-efficient and low-complexity near-field shaping algorithm, yielding improved efficiency by concentrating power in desired radiative near-field areas close to large or distributed antenna arrays. Simultaneously, low field levels are radiated outside these regions through Tikhonov regularization, which additionally minimizes the current magnitudes applied at the antenna feeds, thereby reducing interference and EM- field pollution while enhancing signal quality [9]. Hardware requirements and corresponding costs are lowered by the resulting reduction in transmit power and, moreover, by proposing an algorithm that only relies on phase shifters in the feed network, and that is robust to both amplitude and phase uncertainties.

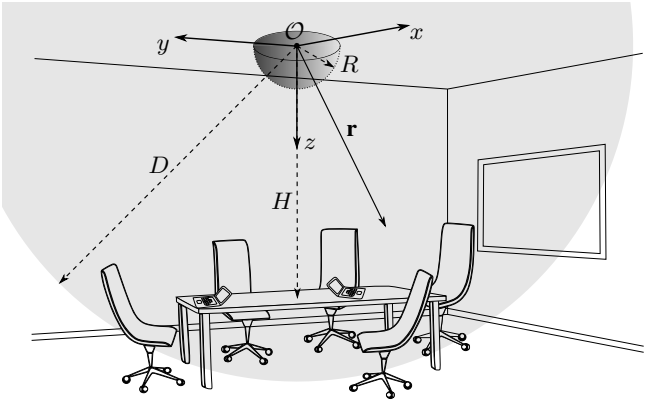

Fig. 1. Application scenario: Multiple receiving devices distributed on a table in the radiative near-field of an antenna array with radius R. The distance H between transmitters and receivers is smaller than the far-field distance $D = 8R^2/\lambda$, with λ the free-space wavelength.

Many existing EM near-field shaping techniques come with drawbacks limiting their applicability. In contrast to [10], the current algorithm produces electric near-fields for any required shape, instead of a spherical target surface. The near-field focusing time-reversal-based method in [11] and [12] keeps undesired secondary lobes within the target region under control, while losing control over the field outside this region of interest. In contrast, the proposed method limits EM-field exposure in these areas by minimizing the antenna feed currents via Tikhonov regularisation. Furthermore, while effective, the method in [13] does not enforce constraints the field's phases, making it less applicable to communication scenarios. In contrast, the advocated algorithm provides a trade-off between focusing accuracy and complexity of the feed network, by introducing a new optimized solution that enables near-field shaping by manipulation of only the feed currents' phases. Finally, in [14] and [15], interference between the basic fields composing more complex shapes generates undesired sidelobes, affecting the quality of the final distribution. In contrast, owing to well-regularized feed currents, the novel solution produces no sidelobes around the target area.

Manuscript received xxx xx, 2023; revised xxx xx, 2023; accepted xxx xx, 2023. Date of publication X; date of current version X.

The authors are with QUEST/Electromagnetics Group, Department of Information Technology, Ghent University-IMEC, IDLab, Technologiepark Zwijnaarde, Ghent B-9052, Belgium (e-mail: Alessandro.Felaco@UGent.be; KamilYavuz.Kapusuz@UGent.be; Hendrik.Rogier@UGent.be; Dries.VandeGinste@UGent.be).

This article has been accepted for publication in IEEE Antennas and Wireless Propagation Letters. This is the author's version which has not been fully edited and content may change prior to final publication. Citation information: DOI 10.1109/LAWP.2024.3355989

II. Least-Squares Near-Field Focusing

Consider the application scenario in Fig. 1, where a number of receive devices are distributed on a planar surface, such as a table, in the radiative near-field of a transmit antenna array, mounted on the ceiling. The array's phase center is the origin of the coordinate system $\mathcal{O}(x, y, z)$, which also coincides with the center of the array's circumscribing sphere of radius R. The distance between the surface and the array center equals H. The array comprises N antenna elements, each excited by a current $i_n \in \mathbb{C}$, with $n = 1, \ldots, N$. Without loss of generalization, we assume that the array is designed such that all the antenna elements exhibit the same polarization. Then, by superposition, the array's radiated co-polar electric field under arbitrary excitation can be written as a weighted sum $e(\mathbf{r}) = \sum_{n=1}^{N} i_n e_n(\mathbf{r})$ of N elementary contributions $e_n(\mathbf{r})$. These are obtained by injecting a $i_n = 1$ A current into the n^{th} array's port via a Norton equivalent source, while terminating all other elements (here by 50 Ω). Through the addition theorem for spherical Hankel functions, each elementary electric field $e_n(\mathbf{r})$ is expanded as

$$e_n(\mathbf{r}) = -jk \sum_{\lambda=0}^{\Lambda} \sum_{\mu=-\lambda}^{\lambda} f_{\lambda,n}^{\mu} \mathcal{H}_{\lambda}^{\mu}(k\mathbf{r}), \tag{1}$$

where $\mathcal{H}_{\lambda}^{\mu}(k\mathbf{r}) = j^{-\lambda} h_{\lambda}^{(2)}(kr) Y_{\lambda}^{\mu}(\hat{\mathbf{r}})$ is the multipole function, with $h_{\lambda}^{(2)}$ the λ^{th} order spherical Hankel function of the second kind [16, p. 437], Y_{λ}^{μ} the λ^{th} order, μ^{th} degree scalar spherical harmonic [17] and $\hat{\mathbf{r}}$ a unit vector. $\mathbf{r}$ is the observation point, with $|\mathbf{r}| = r \geq R$ and k the wavenumber. By expanding the coefficients $f_{\lambda,n}^{\mu}$ into plane waves via the spherical Fourier transform [10, eq. (6)], we obtain an efficient far-to-near-field transformation

$$f_{\lambda,n}^{\mu} = \oiint_{\Omega} F_n(\hat{\mathbf{k}}) \bar{Y}_{\lambda}^{\mu}(\hat{\mathbf{k}}) \, \mathrm{d}\hat{\mathbf{k}}, \tag{2}$$

relating the n^{th} *active* co-polar far-field radiation pattern $F_n(\hat{\mathbf{k}})$, obtained by exciting the n^{th} array element in the same manner as to produce $e_n(\mathbf{r})$, to its respective near field. The applied excitation scheme, which injects a 1 A current into the n^{th} port via a Norton equivalent source, with all other ports terminated [10, Fig. 3], includes all mutual coupling effects, as it allows induced currents to flow in all elements besides the excited antenna. Those currents will enlarge the effective aperture of the antenna array and the corresponding far-field distance beyond that of the stand-alone elements. While standard far-field approximations exploit the radiation pattern F_n along a *single direction*, (2) leverages information originating from *all directions*. For fields outside the sphere circumscribing the array, this enables comprehensive and accurate radiative near-field shaping.

As a representative application, we synthesize the focal pattern $e(\mathbf{r})$ of Fig. 2, mimicking an arbitrary distribution of devices on the table of Fig. 1, with dimensions $8\lambda \times 8\lambda$. To this end, we rely on a planar array operating at 2.45 GHz (with $\lambda \approx 12.5$ cm), consisting of $N = 197$ y-polarized microstrip patch antennas, with dimensions 27×27 mm^2 on a 1.5 mm-thick FR4-substrate, with $\epsilon_r = 4.62$. The presence of a ground plane mitigates reflections of the field radiated

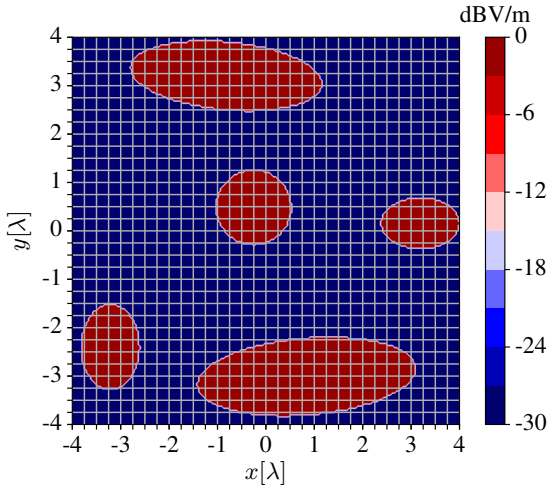

Fig. 2. The target shape $e(\mathbf{r})$ is sampled every $\lambda/4$ in both the x and y directions, for a total of $33 \times 33 = 1089$ sample points.

by the near-field focused array on the ceiling. Moreover, to introduce realistic mutual coupling effects, the antennas are uniformly distributed within a disc of radius $R = 4\lambda \approx 50$ cm with $\lambda/2$ inter-element spacing. The array, whose far-field distance equals $D = 8R^2/\lambda \approx 16$ m, is mounted at a height $H = 12\lambda \approx 1.5$ m $\ll D$ above the target surface. The target shape $e(\mathbf{r})$ is then sampled at a quarter-wavelength spacing in both x and y directions to guarantee uniformity of the target field (Fig. 2). This creates a grid of $33 \times 33 = 1089 = O$ points $\mathbf{r}_o$, with $o = 1, \ldots, O$. Setting $e(\mathbf{r}_o) = e_o$ and (1) yield

$$\sum_{n=1}^{N} z_{on} i_n = e_o \rightarrow \mathbf{Z} \cdot \mathbf{i} = \mathbf{e}, \tag{3}$$

$$z_{on} = -jk \sum_{m=1}^{M} f_{m,n} \mathcal{H}_m(k\mathbf{r}_o), \tag{4}$$

where the vectors $\mathbf{i}$ and $\mathbf{e}$ collect the N currents i_n and the O target field samples e_o, respectively. Hence, the impedance matrix $\mathbf{Z}$ has dimensions $O \times N$, and its elements z_{on} have unit Ω/m. Since $O \gg N$, a solution is obtained via the least-squares method (LSM), minimizing $\epsilon_1 = \|\mathbf{Zi} - \mathbf{e}\|_2^2$:

$$\mathbf{i} = \arg\min_{\mathbf{i}}(\epsilon_1) = \left(\mathbf{Z}^{\dagger}\mathbf{Z}\right)^{-1} \mathbf{Z}^{\dagger} \cdot \mathbf{e}, \tag{5}$$

with $\dagger$ the conjugate transpose.

The resulting electric field's amplitude is shown in Fig. 3a, with $\epsilon_1 \approx 31.2$ and the original shape being reproduced almost flawlessly. However, to achieve this resolution in the target region through interference, currents up to 4.7 kA and a total input power of 8.3 GW are required. This inevitably results in uncontrolled field amplitudes up to 71 dBV/m outside the target plane, yielding unacceptable exposure to users.

III. Tikhonov Regularization

For human bodies in the vicinity of a device producing EM waves, limitations are enforced on the EM energy absorbed per unit mass [18]. Hence, to reduce exposure to EM fields, we improve upon the previous solution by decreasing the input power while approximating the desired resolution as accurately

This article has been accepted for publication in IEEE Antennas and Wireless Propagation Letters. This is the author's version which has not been fully edited and content may change prior to final publication. Citation information: DOI 10.1109/LAWP.2024.3355989

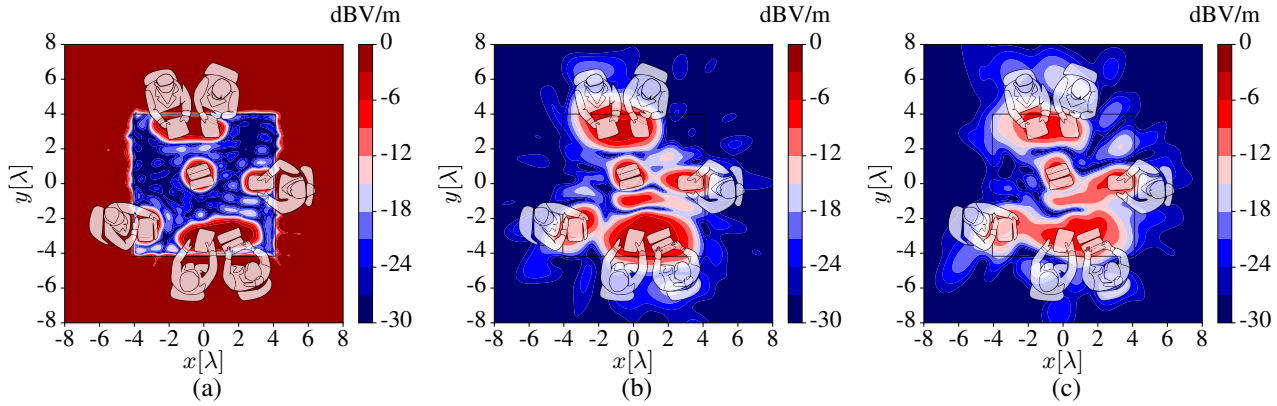

Fig. 3. The target electric near-field of Fig. 2 is obtained via (a) the least-squares method (LSM) ($\epsilon_1 \approx 31.2$), (b) the split regularised LSM (SRLSM) ($\epsilon_4 \approx 117.2$) and (c) the optimized SRLSM (OSRLSM) ($\epsilon_4 \approx 151$). In contrast to (b) and (c), the result in (a) exhibits amplitudes up to 71 dBV/m outside the original target surface, violating specific absorption rate (SAR) regulations [18]. In the figure, field levels are normalized to 0 dBV/m for readability.

as possible. Therefore, we solve (5) while simultaneously limiting the norm of $\mathbf{i}$. This is achieved by applying the *regularised* least-squares method (RLSM) [19], which modifies ϵ_1 to $\epsilon_2 = \epsilon_1 + \|\mathbf{\Gamma i}\|_2^2 = \|\mathbf{Zi} - \mathbf{e}\|_2^2 + \|\mathbf{\Gamma i}\|_2^2$ and (5) to

$$\mathbf{i} = \arg\min_{\mathbf{i}}(\epsilon_2) = \left(\mathbf{Z}^\dagger\mathbf{Z} + \mathbf{\Gamma}^\dagger\mathbf{\Gamma}\right)^{-1}\mathbf{Z}^\dagger \cdot \mathbf{e}, \tag{6}$$

with $\mathbf{\Gamma}$ the Tikhonov matrix, commonly chosen to be a scalar matrix $\mathbf{\Gamma} = \alpha\mathbf{I}$. This regularization improves the conditioning of the original problem and, hence, lowers power consumption, by offsetting the small eigenvalues of $\mathbf{Z}^\dagger\mathbf{Z}$ by a Tikhonov factor α [20]. Thereby, the model produces smaller current amplitudes, as it minimizes $\epsilon_3 = \|\mathbf{Zi} - \mathbf{e}\|_2^2 + \alpha\|\mathbf{i}\|_2^2$, which reduces the original error ϵ_1 while enforcing the constraint on the currents' amplitudes via the factor $\alpha \geq 1$, increasing the likelihood of obtaining solutions with smaller norms. Still, this procedure acts blindly on all currents, regardless of their contribution to the electric field produced in the target region.

To refine the solution, we split the set of samples in two parts. The first group includes the O_ζ samples inside the red focal spots of Fig. 2. The second group collects the remaining O_η samples, so that $O = O_\zeta + O_\eta$. Accordingly, we also split the impedance matrix into two blocks. The first submatrix $\boldsymbol{\zeta}$ maps the currents $\mathbf{i}$ to the O_ζ electric field values $\boldsymbol{\zeta}\mathbf{i}$ within the focal spots. These values are required to match the target $\mathbf{e}$ in both amplitude and phase, which is equivalent to minimizing $\|\boldsymbol{\zeta}\mathbf{i} - \mathbf{e}\|_2^2$. The second submatrix $\boldsymbol{\eta}$ maps the currents $\mathbf{i}$ to remaining O_η electric field values within the shadow (blue) regions. These are simply required to have minimal amplitude, which is equivalent to minimizing $\|\boldsymbol{\eta}\mathbf{i}\|_2^2$. The diagonal elements of $\boldsymbol{\eta}^\dagger\boldsymbol{\eta}$ are of the form $\left[\boldsymbol{\eta}^\dagger\boldsymbol{\eta}\right]_{nn} = \sum_{o=1}^{O_\eta}|\eta_{no}|_2^2$, which is a *measure of the excess radiation produced by the n^{th} array element in the shadow regions*. Therefore, we choose the Tikhonov matrix as

$$\mathbf{\Gamma} = \alpha\left[\text{diag}\left(\boldsymbol{\eta}^\dagger\boldsymbol{\eta}\right)\right]^{\frac{1}{2}}, \tag{7}$$

such that a higher or lower n^{th} diagonal value of $\mathbf{\Gamma}$ increases or reduces, respectively, the sensitivity of the n^{th} current to regularization via ϵ_2. This leads to the following final formulation for the *split* regularised least-squares method (SRLSM):

$$\mathbf{i} = \arg\min_{\mathbf{i}}(\epsilon) = \left[\boldsymbol{\zeta}^\dagger\boldsymbol{\zeta} + \alpha\,\text{diag}\left(\boldsymbol{\eta}^\dagger\boldsymbol{\eta}\right)\right]^{-1}\boldsymbol{\zeta}^\dagger \cdot \mathbf{e}, \tag{8}$$

$$\epsilon_4 = \|\boldsymbol{\zeta}\mathbf{i} - \mathbf{e}\|_2^2 + \alpha\left\|\left[\text{diag}\left(\boldsymbol{\eta}^\dagger\boldsymbol{\eta}\right)\right]^{\frac{1}{2}}\mathbf{i}\right\|_2^2, \tag{9}$$

where, again, the Tikhonov factor α is used for fine-tuning.

The electric field generated by solving (8), with α = 2 and where $\epsilon_4 \approx 117.2$, is shown in Fig. 3b. The computation required circa 1 s on an Intel Core i7-8650U running at 1.90 GHz with 16 GB RAM. On the one hand, a small price is paid in terms of sharp reproduction of the focal patterns. On the other hand, this trade-off permits to drastically reduce the maximum current's magnitude from 4.7 kA down to 1.2 mA, consequentially reducing the input power from 8.3 GW down to 1.4 mW. This both prevents undesired focusing outside the target region, reducing the EM exposure of the users, and dramatically increases the radiation efficiency. Moreover, owing to both an adequate inter-element spacing and a well-conditioned solution, no sidelobes are produced around the target area of Fig. 3b.

IV. Equi-amplitude Solution

The solution proposed in the previous section is more than satisfying for any application requiring fast and efficient focusing of EM power in the radiative near-field. However, implementing an intricate feeding network to generate the feed currents is not only expensive, but also introduces errors due to limited amplitude and phase resolution. To partially mitigate this issue, an equi-amplitude solution, with all currents having the same magnitude and only steered in phase, is now presented. This alternative result is coined the *optimized* split regularised least-squares method (OSRLSM).

Starting from the solution in previous section, we now perform an extra optimization step with an additional constraint:

$$\mathbf{i} = \arg\min_{\mathbf{i}}\left(\|\boldsymbol{\zeta}\mathbf{i} - \mathbf{e}\|_2^2 + \alpha\left\|\left[\text{diag}\left(\boldsymbol{\eta}^\dagger\boldsymbol{\eta}\right)\right]^{\frac{1}{2}}\mathbf{i}\right\|_2^2\right), \quad \text{subject to } |i_n|_2 = A \in \mathbb{R} > 0,\ \forall n = 1, \ldots, N \tag{10}$$

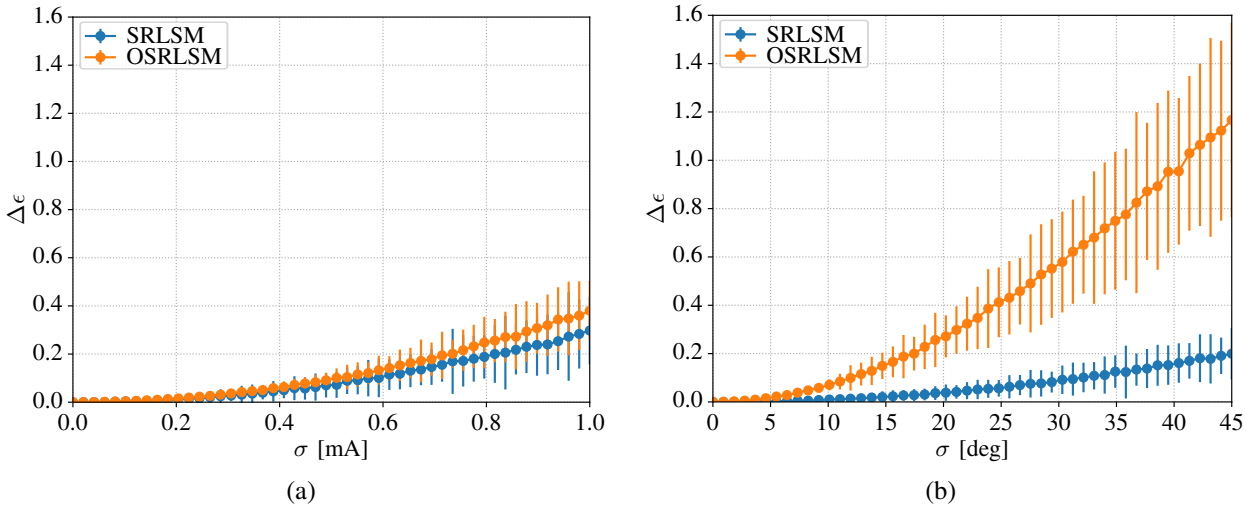

Fig. 4. Stability to (a) amplitude and (b) phase perturbations σ of the regularised least-squares method (SRLSM) solution (8) and its optimized version (OSRLSM) (10). The former shows a very robust behavior to relatively large amplitude or phase perturbations. while the latter shows a higher sensitivity to phase variations owing to the reduced amount of degrees of freedom.

where A is a positive real number representing the common current amplitude. In practice, the OSRLSM optimizes the feed currents' phases given by the already close-to-optimal solution provided by (8), with the objective of minimizing the error function (9). This is achieved by applying Powell's conjugate direction algorithm [21], which allows to also enforce the same amplitude for all the feed currents. Computationally, this slightly increases the CPU time, while providing phase-only control of the electric near-field.

This solution (Fig. 3c) produces currents with amplitude $A \approx 0.4$ mA, and input power of 0.9 mW after a computation time of 1.8 s due to extra optimization. By reducing the number of degrees of freedom from $2N$ to $N+1$, an increased focusing error ($\epsilon_4 \approx 151$) is expected. Still, the overall target pattern is very well retained when steering only the currents' phases for the near-field shaping. Moreover, this phase-only near-field shaping reduces hardware requirements, leading to a more robust and cost-effective feed-network implementation.

V. Robustness

To study the robustness of both (8) and (10) against variations in the currents' amplitude and phases, we analyze the relative variation $\Delta\epsilon = \frac{\epsilon(\sigma)-\epsilon_0}{\epsilon_0}$ of the error (9) to a perturbation σ, with $\epsilon\,(\sigma = 0) = \epsilon_0$ the unperturbed error. In Fig. 4a we study the stability to amplitude variations. The currents' magnitudes are assumed to be distributed according to a set of N independent random variables following the Gaussian probability density function $\phi_n(x) = \frac{1}{\sqrt{2\pi\sigma^2}} e^{-\frac{1}{2}\left(\frac{x-\mu_n}{\sigma}\right)^2}$, with the mean μ_n the unperturbed values of Fig. 3b and Fig. 3c, and the perturbation σ the standard deviation. In the process, the feeding currents' phases remain fixed to their unperturbed values, yielding Fig. 3b and Fig. 3c. In Fig. 4b, we study the stability to phase variations instead, by switching the roles of amplitude and phase. The intervals covered by σ in Fig. 4, up to 1 mA for the amplitude and 45° for the phase, were chosen to reproduce the worst possible operating conditions. For each σ value in Fig. 4, 100 experiments were performed. The range covered by the relative error $\Delta\epsilon$ is shown as an error bar, and its average as a dot. The SRLSM solution (8) of Section III proves very robust to relatively large amplitude and phase perturbations. Even under the worst conditions, the relative error increases by just 25%, further reducing hardware costs and complexity owing to a reduced need for high-precision components. As expected, while being robust to amplitude variations, the OSRLSM solution (10) provided in Section IV shows a higher sensitivity to phase variations.

VI. Conclusions & Future Work

A novel method was proposed to accurate and efficiently generate a near-field focal pattern using a planar antenna array topology. Contrary to existing techniques, the algorithm provides accurate near-field focusing in terms of amplitude and phase of the co-polar electric field, in the presence of mutual coupling based on the antenna elements' active far-field patterns, translated to near-field data via a spherical Fourier transform and multipole expansion. Owing to the minimization of transmit power by Tikhonov regularization, by steering through phase shifters only and by enhanced robustness to amplitude and phase steering errors, the approach exhibits improved applicability and a reduction in feed network complexity over existing techniques. In a representative use-case scenario, accurate shaping within a planar surface located in the array's radiative near-field region is achieved, preventing undesired radiation outside the target region. Owing to its efficiency, the novel method is an optimal candidate for real-time near-field shaping applications.

To improve the proposed algorithm's accuracy, future work includes replacing the free-space Green's function by a system impulse response that accounts for all radiowave propagation aspects in the environment under study. In indoor applications, this entails, among others, including reflections on the side walls and the floor. Also the presence of mobile users can be added, at the cost of increasing the algorithm's complexity and making signal processing more power-consuming.

REFERENCES

[1] H. Holma, H. Viswanathan, and P. Mogensen, "Extreme massive MIMO for macro cell capacity boost in 5G-Advanced and 6G," *Nokia Bell Labs White Paper*, 2021.

[2] W. Chen et al., "5G-Advanced Toward 6G: Past, Present, and Future," *IEEE J. Sel. Areas Commun.*, vol. 41, no. 6, pp. 1592-1619, Jun. 2023.

[3] M. Cui and L. Dai, "Channel estimation for extremely large-scale MIMO: Far-field or near-field?" *IEEE Trans. Commun.*, vol. 70, no. 4, pp. 2663–2677, Apr. 2022.

[4] T. S. Rappaport, "Wireless communications and applications above 100 GHz: Opportunities and challenges for 6G and beyond," *IEEE Access*, vol. 7, pp. 78729-78757, 2019.

[5] G. Bacci, L. Sanguinetti, and E. Björnson, "Spherical wavefronts improve MU-MIMO spectral efficiency when using electrically large arrays," *IEEE Wireless Commun. Lett.*, vol. 12, no. 7, pp. 1219-1223, Jul. 2023.

[6] G. G. Bellizzi, M. T. Bevacqua, L. Crocco, and T. Isernia, "3-D field intensity shaping via optimized multi-target time reversal," *IEEE Trans. Antennas Propag.*, vol. 66, no. 8, pp. 4380-4385, Aug. 2018.

[7] D. Zhao and M. Zhu, "Generating microwave spatial fields with arbitrary patterns," *IEEE Antennas Wireless Propag. Lett.*, vol. 15, pp. 1739-1742, Feb. 2016.

[8] W. Geyi, "The method of maximum power transmission efficiency for the design of antenna arrays," *IEEE Open J. Antennas Propag.*, vol. 2, pp. 412-430, Mar. 2021.

[9] F. F. Manzillo and M. Defives, "Synthesis of transmitarrays for far-and near-field shaping using convex optimization," in *Proc. Eur. Conf. on Antennas and Propag.*, Florence, Italy, Mar. 2023, pp. 1-5.

[10] A. Felaco, K. Y. Kapusuz, H. Rogier, and D. Vande Ginste, "Spherical Fourier-transform-based real-time near-field shaping and focusing in beyond-5G networks," *MDPI Sensors*, vol. 23, no. 6, pp. 3323-3340, Mar. 2023.

[11] G. G. Bellizzi, D. A. M. Iero, L. Crocco, and T. Isernia, "Three dimensional field intensity shaping: The scalar case," *IEEE Antennas Wirel. Propag. Lett.*, vol. 17, no. 3, pp. 360-363, Jan. 2018.

[12] G. G. Bellizzi and M. T. Bevacqua, "The linear sampling method as a tool for "blind" field intensity shaping," *IEEE Trans. Antennas Propag.*, vol. 68, no. 4, pp. 3154–3162, Jan. 2020.

[13] J. W. Wu, R. Y. Wu, X. C. Bo, L. Bao, X. J. Fu, and T. J. Cui, "Synthesis algorithm for near-field power pattern control and its experimental verification via metasurfaces," *IEEE Trans. Antennas Propag.*, vol. 67, no. 2, pp. 1073-1083, Nov. 2018.

[14] S. Guo, D. Zhao, B. Z. Wang, and W. Cao, "Shaping electric field intensity via angular spectrum projection and the linear superposition principle," *IEEE Trans. Antennas Propag.*, vol. 68, no. 12, pp. 8249-8254, May 2020.

[15] R. Liu and K. Wu, "Antenna array for amplitude and phase specified near-field multifocus," *IEEE Trans. Antennas Propag.*, vol. 67, no. 5, pp. 3140-3150, Feb. 2019.

[16] M. Abramowitz and I. A. Stegun, *Handbook of Mathematical Functions with Formulas, Graphs, and Mathematical Tables,* US Government printing office, vol. 55, 1964.

[17] J. Rahola, F. Belloni, and A. Richter, "Modelling of radiation patterns using scalar spherical harmonics with vector coefficients," in *Proc. Eur. Conf. Antennas and Propag.*, Berlin, Germany, Mar. 2009, pp. 3361-3365.

[18] G. Ahmed *et al.*, "Rigorous analysis and evaluation of specific absorption rate (SAR) for mobile multimedia healthcare," *IEEE Access*, vol. 6, pp. 29602-29610, May 2018.

[19] D. Calvetti and L. Reichel, "Tikhonov regularization of large linear problems," *BIT Numerical Mathematics*, vol. 43, pp. 263-283, Jun. 2003.

[20] Massachusetts Institute of Technology notes. [Online]. Available: https://bit.ly/3eQadN4 https://www.mit.edu/ 9.520/scribe-notes/cl7.pdf

[21] M. J. D. Powell, "An efficient method for finding the minimum of a function of several variables without calculating derivatives", *The Comp. J.*, vol. 7, no. 2, pp. 155-162, Jan. 1964.